doi:10.1093/mnras/sty038

MNRAS **475**, 4367–4377 (2018) Advance Access publication 2018 January 8

The structure and spectrum of the accretion shock in the atmospheres of young stars

Alexandr Dodin*

Sternberg Astronomical Institute, Moscow M.V. Lomonosov State University, Universitetskij pr., 13, Moscow, 119992, Russia

Accepted 2018 January 2. Received 2018 January 2; in original form 2017 September 25

ABSTRACT

The structure and spectrum of the accretion shock have been self-consistently simulated for a wide range of parameters typical for Classical T Tauri Stars (CTTS). Radiative cooling of the shocked gas was calculated, taking into account the self-absorption and non-equilibrium (timedependent) effects in the level populations. These effects modify the standard cooling curve for an optically thin plasma in coronal equilibrium, however the shape of high-temperature $(T > 3 \times 10^5 \,\mathrm{K})$ part of the curve remains unchanged. The applied methods allow us to smoothly describe the transition from the cooling flow to the hydrostatic stellar atmosphere. Thanks to this approach, it has been found that the narrow component of He II lines is formed predominantly in the irradiated stationary atmosphere (hotspot), i.e. at velocities of the settling gas <2 km s⁻¹. The structure of the pre-shock region is calculated simultaneously with the heated atmosphere. The simulation shows that the pre-shock gas produces a noticeable emission component in He II lines and practically does not manifest itself in He I lines (λλ 5876, 10830 Å). The ultraviolet spectrum of the hotspot is distorted by the pre-shock gas, namely numerous red-shifted emission and absorption lines overlap each other forming a pseudocontinuum. The spectrum of the accretion region at high pre-shock densities $\sim 10^{14}$ cm⁻³ is fully formed in the in-falling gas and can be qualitatively described as a spectrum of a star with an effective temperature derived from the Stefan–Boltzmann law via the full energy flux.

Key words: accretion, accretion discs – radiative transfer – shock waves – stars: atmospheres – stars: variables: T Tauri, Herbig Ae/Be.

1 INTRODUCTION

Classical T Tauri stars (CTTS) are young low-mass stars, accreting matter from a protoplanetary disc. According to the current paradigm (see e.g. the review by Hartmann, Herczeg & Calvet 2016), the observational properties of these stars can be explained in the frame of a magnetospheric accretion scenario (Koenigl 1991; Romanova et al. 2003). In this model, the accretion flow at distances smaller than a few stellar radii is governed by a strong stellar magnetic field. Falling down towards the star along the field lines, the plasma is accelerated up to the free-fall velocity at the stellar surface. The kinetic energy of the flow is converted into heat in the strong shock and escapes in the form of radiation.

The radiation from the shock cooling region, concentrated mainly in the ultraviolet (UV) and X-ray regions, irradiates the stellar atmosphere on one side and the free-falling gas on the other side of the shock. Calvet & Gullbring (1998) and Dodin & Lamzin (2012) have shown that the heated atmosphere or, in other words, the hotspot is a source of continuous emission and numerous emission lines, which reduce the depths of absorption lines in the spectra of CTTS

compared to the spectra of main-sequence stars of the same spectral types. Matching the observed excess emission in the visible and UV regions with a suitable model is the main method used for the determination of the accretion rates (Ingleby et al. 2013). Note that the accretion rate is measured only on visible part of the stellar surface and can differ from the total accretion rate, but if the rotational axis of the star allows observation of most of the surface, then the total accretion rate can be retrieved from spectra obtained at various rotational phases. Certainly, this requires a stationary picture of accretion, which is probably not always realized (Blinova, Romanova & Lovelace 2016). Nevertheless, there are stars where the spectral accretion signatures are stable on time-scales of a few rotational periods; one example is V2129 Oph (Alencar et al. 2012). The stable accretion and dense phase coverage allow one to not only deduce the rotational modulation of the accretion rate, but also obtain a map of accretion parameters on the stellar surface by using the Doppler imaging technique (Piskunov, Tuominen & Vilhu 1990). To apply this technique, it is necessary to know an angular distribution of specific intensity $I_{\nu}(\mu)$ for each line involved in the analysis. The efficiency of this approach has already been demonstrated in the magnetic mapping of young stars (see e.g. Donati et al. 2007, 2008, 2011, 2013). However, it should be noted that magnetic imaging has been carried out without proper account for a hotspot, which

^{*} E-mail: dodin_nv@mail.ru

can distort the obtained results. The specific intensity I_{ν} (μ) for the hotspot has been recently calculated by Dodin & Lamzin (2012) and Dodin (2015); the current work is in part a continuation that more accurately treats the radiation, which heats the hotspot, and includes self-consistently the pre-shock, which probably begins to dominate in the spectrum at the pre-shock densities $N_0 \sim 10^{13}$ cm⁻³ (Lamzin 1995). But even at moderate densities, the in-falling gas manifests itself in spectra as a red-shifted component of some strong lines [e.g. C IV λ 1550 Å, He II λ 1640 Å (Ardila et al. 2013), He I λ 5876 Å, O I λ 7773 Å (Petrov et al. 2001), and other lines]. Large Doppler shifts of these components make them informative for a diagnostic of the accretion geometry; however, to make such a diagnostic, a quantitative theory of formation of these components should be constructed. The above serves as a motivation for a detailed calculation of the structure and spectrum of the pre-shock region.

There are several works dedicated to the modelling of spectral lines in the free-falling gas. Muzerolle, Calvet & Hartmann (2001), Kurosawa & Romanova (2013) have considered the formation of H I and Na I lines in the accretion column far from the shock front. The important limitation of these models is an uncertainty in the calculation of the thermal structure, related to the unknown processes responsible for the gas heating. Whatever the processes were, the temperatures considered in these models <10 000 K allow us to reproduce the observed inverse P-Cygni profiles of H I and Na I, but cannot produce 'hot lines' such as He I–II, C IV. In the case of He I, this problem can, in principle, be solved if we include in the calculation coronal X-rays, even small amounts of which can lead to appearance of He I lines (Kurosawa, Romanova & Harries 2011).

It is natural to suppose that the hot lines should be formed in the pre-shock region irradiated by the shock emission. Line formation in the pre-shock region due to photoionization has been considered by Lamzin (2003), who has calculated the specific intensity $I_{\nu}(\mu)$ for some emission lines. In our work, we present a new model of the shock region, which takes into account the line and continuum emission originating from the pre-shock and post-shock regions as well as the hotspot. The in-falling gas is irradiated by the same radiation as the heated atmosphere; moreover, both regions have similar physical parameters and as a consequence, the emergent spectra of these regions are similar, i.e. they can absorb and reemit radiation of each other. To take into account this radiative interaction, both regions will be calculated simultaneously.

The ionizing radiation of the post-shock has already been calculated by Lamzin (1998) and has been used in previous work dedicated to the modelling of the hotspot (Dodin 2015). However, this radiation is given in the form of flux F_{ν} , while we need a specific intensity $I_{\nu}(\mu)$ (see discussion in Dodin 2015). The angular distribution of $I_{\nu}(\mu)$ is not universal for the whole spectrum, but depends on the optical thickness at each frequency. To obtain the correct angular distribution, a new calculation of the post-shock is needed.

The necessity of such calculations is also caused by the fact that the post-shock smoothly passes in the heated atmosphere, while in previous studies (e.g. Lamzin 1998; Dodin 2015) these regions were simulated separately by substantially different methods. An ambiguity of the division into these regions leads to uncertainties in the line profiles formed on their boundary, such as C IV, He II, etc. In the other words, works dedicated to the modelling of the post-shock spectra do not take into account the contribution of the heated atmosphere and vice versa. Here, we consider a model in which the cooling flow and the stellar atmosphere are calculated in a single approach that allows us to reach a smooth transition from one to another.

To calculate the ionizing radiation, we will suppose that the shock is stationary. On the one hand, the theory predicts (Koldoba et al. 2008; Sacco et al. 2008) that the shock must be unstable in the case of the standard cooling curve for an optically thin plasma; on the other hand, recent observational data of young stars do not show any evidence of such an instability (Drake et al. 2009; Günther et al. 2010). The absence of observed manifestations of the instability can be explained if the shock is not uniform. Due to the strong magnetic field, the accretion flow can be represented as a set of flux tubes, in each of which the shock front oscillates independently of the others. Moreover, the frequencies of these oscillations may differ if the gas densities in these tubes differ (Matsakos et al. 2013). An alternative explanation for the absence of the instability is the difference between the real cooling curve and the standard one. The most obvious causes of such deviations are non-equilibrium (timedependent) effects in the level populations (Sutherland & Dopita 1993; Lamzin 1998) and self-absorption of the produced radiation. In the present work, we will consider how these effects transform the cooling curve.

2 MODELLING THE STRUCTURE OF THE POST-SHOCK REGION

The steady-state cooling flow is modelled by solving HD equations of conservation of mass, momentum, and energy:

$$\rho V = \rho_0 V_0 \equiv u_0,\tag{1}$$

$$P + \rho V^2 = \rho_0 V_0^2 + P_0, \tag{2}$$

$$u_0 \frac{\mathrm{d}E}{\mathrm{d}m} = H - C. \tag{3}$$

Gravity and heat conductivity are neglected. Here ρ is the mass density. Alternatively, we will use a number density N, which is related to ρ as: $\rho = 2.11 \times 10^{-24} (\mathrm{g}) \times N$, for the solar elemental abundances. V is the plasma velocity; P is the thermal pressure; and m is the mass coordinate. We denote the pre-shock values by subscript 0. E is the specific energy, which for an ideal monatomic gas can be expressed as

$$E = \frac{V^2}{2} + \frac{5}{2} \frac{P}{\rho} + \varepsilon,\tag{4}$$

$$\varepsilon = \frac{1}{\rho} \sum_{l} N_{l} E_{l},\tag{5}$$

where N_l are the populations of all atomic levels of all elements in all ionization stages, and E_l are the energies of the levels. The variables $H = 4\pi \int \chi_{\nu} J_{\nu} d\nu$, $C = 4\pi \int \chi_{\nu} S_{\nu} d\nu$ are the heating and cooling rates of the gas per unit mass. χ_{ν} , J_{ν} , and S_{ν} denote correspondingly the opacity, the mean intensity, and the source function at the frequency ν .

The radiation field is determined by the radiative transfer equation (RTE), which is solved by the short characteristic method (Olson & Kunasz 1987). The spectra are calculated from 1 Å to 230 μm on an adaptive grid with $\sim\!10^5$ frequency points. The Thomson optical thickness for all models is $<\!10^{-4}$, therefore the scattering on free electrons is negligible and ignored.

Because in the cooling flow the statistical equilibrium (SE) may be absent, to calculate the fractional level populations n_i the corresponding system of ODEs for each chemical element should be

solved

$$u_0 \frac{\mathrm{d}n_i}{\mathrm{d}m} = \sum_{j=1}^K (R_{ji} + C_{ji}) n_j - n_i \sum_{j=1}^K (R_{ij} + C_{ij}),$$

$$i = 1, K - 1, \qquad \sum_{i=1}^K n_i = 1,$$
(6)

where K is the number of the last considered level, i.e. the ground state of the last considered ionization stage of the element. R_{ij} and C_{ij} are the radiative and collisional rate coefficients from level i to level j. After n_K is expressed from the last equation via the rest of the n_i , the system of stiff differential equations are solved by using a variable-coefficient ordinary differential equation solver (Brown, Byrne & Hindmarsh 1989). Recall that the populations in SE are defined by linear equations, which are obtained from equation (6) by setting $u_0 \frac{dn_i}{dm} = 0$. Finally, the level populations are calculated as follows $N_i = \xi_{\rm el} N n_i$, where $\xi_{\rm el}$ is the abundance of the element el; N is the number density of all atoms and ions. The self-consistent solution of the RTE and equation (6) is achieved by the accelerated Λ -iteration method.

To calculate the temperature distribution T(m) in the post-shock region that satisfies equations (1–3), the modified Λ -correction (Dodin 2017) can be applied. However, simulations with this correction scheme show that temperature in the region of interest drops monotonically, which allows the use of a more simple method. Satisfaction of equation (3) is achieved by calculation of the mass coordinates m(T), which correspond to the predefined temperature grid evenly spaced on a logarithmic scale from T_{max} to T_{min} . The coordinates m are calculated from the equation (3), which can be rewritten as

$$dm = \frac{u_0}{H - C} dE, \tag{7}$$

where the right-hand side is known from the previous iteration. The convergence is usually reached after five iterations. $T_{\rm max}$ is defined from the initial conditions at the shock front. $T_{\rm min}$ is determined by the condition that the gas reaches the radiative equilibrium ($H \approx C$). As we will see later, the gas, cooled down to $T_{\rm min}$, loses almost all its velocity ($V \lesssim 1~{\rm km\,s^{-1}}$) and reaches not only the radiative equilibrium but also the SE, i.e. below this temperature the gas can indeed be considered as a part of the hotspot (see the next section).

Generally speaking, just behind the shock front the electron and ion temperatures are different. But in the regions where this difference is significant, the gas emits a negligible ($\lesssim 10^{-3}$) part of its energy (Lamzin 1998). We do not consider such thin structures at the shock front, which allows us to simplify the simulation.

2.1 The initial conditions

The post-shock cooling zone is linked to the models of the preshock gas and hotspot by the initial conditions for the equations (6) and (7) and the RTE.

Obviously, the level populations just before the shock should be taken as initial conditions for equation (6). However, it turned out that just behind the shock, the populations reach equilibrium values at short distances due to high collisional ionization rates. The distance where this equilibration occurs nearly corresponds to the distance where the electron and ion temperatures become equal. This coincidence is not accidental, because both scales are determined by the time of electron—ion collisions. Because for our simulation this region can be ignored, we set the SE populations as initial conditions for equation (6). The initial values of the variables V, P, and ρ are determined by the jump conditions (see Appendix A). The initial velocity is

$$V_{\rm in} \approx \frac{V_0}{4} \left(1 + 5 \frac{P_0}{\rho_0 V_0^2} - \frac{8}{3} \frac{\varepsilon_{\rm in} - \varepsilon_0}{V_0^2} \right),$$
 (8)

where the last correction is due to the fact that when the gas reaches the first grid node, some part of its thermal energy has been spent on ionization and excitation of atoms and ions. The pre-shock values P_0 at the first calculation are set to zero and become known when the pre-shock model is calculated. $P_{\rm in}$ and $\rho_{\rm in}$ are easily calculated from equations (1) and (2), and the initial temperature $T_{\rm max}$ is deduced from the ideal gas equation $P = (N + N_{\rm e})kT$. The initial condition for the energy equation (7) can be obtained from equation (4) for the pre-shock parameters.

The initial condition for the RTE at the shock front is the intensity emerging from the pre-shock towards the star, and for the opposite boundary of the cooling flow it is the intensity emerging from the heated atmosphere. Because the hot gas is mostly transparent for the radiation from the hotspot, these conditions have almost no effect on the structure of the shock wave but allow a more smooth transition for the level populations from the cooling flow to the hotspot to be obtained. At the first step, while the models of the free-falling gas and hotspot are not constructed, we assume that these regions do not emit and have a zero temperature that allows calculation of the structure and spectrum of the cooling flow, and then calculation of the structure and spectrum of the pre-shock gas and hotspot, and a recalculation of the cooling flow with new initial conditions. To reach convergence and a smooth transition at the conventional boundary between the cooling flow and the hotspot, it is sufficient to perform 2-3 such global iterations. All three regions can, in principle, be calculated together, however, we isolate the calculation of the cooling zone in a separate unit, which is linked with surroundings through the boundary conditions. This complication is necessary due to different convergence rates of the post-shock model and pre-shock-hotspot model. The calculation of the post-shock model takes about 10 times fewer Λ -iterations than the pre-shock-hotspot model, but each such iteration is about 100 times longer. Thus, the separation of the code into two units greatly reduces CPU time.

3 MODELLING THE STRUCTURE OF THE PRE-SHOCK REGION AND THE HEATED ATMOSPHERE

Using well-developed methods of the theory of stellar atmospheres, Dodin (2015) has calculated the non-LTE structure and spectrum of the hotspot, taking the pre-shock gas into account in a simplified manner. In this work, we perform a simultaneous calculation of both regions by using the same methods as in Dodin (2015). Referring to this paper for details, we recall the main assumptions used for the modelling. The geometry is plane-parallel. The thermal structure is determined by the radiative equilibrium. The level populations of H, He, C, and O are in SE, while the rest of the elements (from Li to Zn) are in LTE. In this paper, we will mainly concentrate on the spectra of hydrogen and helium, whereas the departures from LTE for C and O will be considered only for accounting for their impact on the H and He lines. The RTE is solved including line and continuum opacity sources, scattering is neglected.

All equations and methods are the same for both regions except for the equation of hydrostatic equilibrium, which is solved for the hotspot only, while the pre-shock is considered as a slab of gas with constant density and velocity. An optically and geometrically thin source of ionizing radiation is placed between the pre-shock and hotspot. The intensity of ionizing radiation $I_{\nu}^{\rm sh}(\mu)$ is calculated by the methods described in the previous section. The shock radiation ionizes and heats the surroundings, which also begin to radiate, predominantly in the UV and visible spectral regions. In order to perform the simultaneous calculation of the pre-shock and the hotspot, the numerical solution scheme of the RTE is modified in such a way that the intensity of the ionizing radiation $I_{\nu}^{sh}(\mu)$ is added to the hotspot radiation (for $\mu>0$) or to the pre-shock radiation ($\mu<0$) at a depth located between the last grid point of the pre-shock and the first point of the hotspot.

3.1 The doppler shifts

Because two regions move towards each other, the radiation of each, observed from the opposite, is blue-shifted by $\Delta \nu = \nu V_0 \mu/c$, where $\mu > 0$ is the cosine of the angle between the direction of light propagation and the velocity vector, which is parallel to the normal, therefore this μ coincides with $|\mu|$ in the RTE.

As in Dodin (2015), to take into account the line blanketing, we use the opacity sampling technique, which consists of choosing a fixed grid of 10⁴-10⁵ frequencies. This grid is too coarse for the calculation of the spectrum, but is sufficient for accounting for the line opacity. In an addition to this grid, the lines of elements, treated in non-LTE, are calculated on a special grid for each line. This method can be easily applied to our case of moving gas, if we define a dynamic grid for μ for each frequency v_i by the relation $\mu_k = (\nu_{i+k} - \nu_i)c/V_0$ in which k starts from 0 and the last k is determined by the condition $\mu_k < 1$. Even for the usual number of frequency points (>30 000), the angular grid is sufficiently dense to compute various moments of the radiation field. The RTE along each μ is solved by the short characteristic method (Olson & Kunasz 1987). The outgoing intensity is calculated separately in a similar way for a narrow region and with high resolution by using the pre-calculated level population and thermal structure.

To clarify the importance of the Doppler shifts in the calculation of models and spectra, a few test models that cover our parameter range have been calculated for three cases. Case 1: The Doppler shifts are taken into account only for the outgoing spectrum, while the thermal structure and level populations are calculated without the shifts. The set of angles μ in this case are defined by the three-point Gaussian quadrature rule (as in Dodin 2015). Case 2: The Doppler shifts are included in the calculations of the level populations and outgoing spectrum; the thermal structure is taken from Case 1. Case 3: The shifts are considered at all stages. The comparison between Cases 1 and 2 shows that the outgoing fluxes H_{ν} of helium lines can differ by up to a factor of 2, while the same for Cases 2 and 3 gives a difference less than 10 per cent. Therefore, we can use with sufficient accuracy Case 2.

3.2 Non-equilibrium effects

We suppose that the both regions are in radiative equilibrium, and the level populations of elements treated in non-LTE are in SE. As we will see later (see Section 5.1), these conditions are satisfied for the hotspot, because on its upper boundary the cooling gas reaches these equilibriums with sufficient accuracy. In the case of the free-falling gas, this question deserves a separate consideration. We suppose that the pre-shock gas is initially cold and neutral, therefore some time is needed to heat and ionize it. To study the delay in the heating and ionization of the pre-shock gas, the temperature is calculated by using the modified Λ -correction scheme

(Dodin 2017), and the level populations are calculated by solving equation (6). It has been shown by a few test models that the shift of the temperature distribution is significant only for models with very low accretion flux $F_{\rm acc} \approx \rho_0 V_0^3/2$, but even in this case the line profiles of H and He do not differ from those calculated in models in radiative equilibrium. The non-equilibrium effects in the level populations appear only in the H I region, in which helium lines are not formed. Note that the size of the H II region remains practically the same as in the equilibrium case. Therefore, we can conclude that the non-equilibrium effects are more noticeable for low accretion fluxes $F_{\rm acc}$, but for our parameter range they are small and will be ignored.

3.3 Model limitations

As in Dodin (2015), we use a one-dimensional plane-parallel approximation, therefore we can consider only those layers for which the thickness H is smaller than the stellar radius $R \sim 10^{11}$ cm and the accretion column width $D \sim 10^{10}$ – 10^{11} cm, because the larger the ratio H/D, the more radiation escapes through the sides of the accretion column. Although we will consider models with $H=10^{10}$ – 4×10^{10} cm, all quantitative conclusions will concern the lines that are formed in layers with $H\lesssim10^9$ cm, except for extreme models of the lowest density $N_0=10^{10}$ cm⁻³ and the highest velocity $V_0=500\,\mathrm{km\,s^{-1}}$.

Generally speaking, there is a velocity gradient in the free-falling gas such that the velocity difference between the upper and lower boundaries of the slab is $0.5V_0H/R$. In the case of the helium line formation region with $H \sim 10^9$ cm (see Section 5.2), the difference is about $2\,\mathrm{km\,s^{-1}}$, which is comparable with the thermal velocities in the gas; therefore, we suppose that we can neglect the velocity gradient.

We consider the steady-state problem, and therefore cannot directly take into account non-stationary effects of the shock on the spectrum of the hotspot or the pre-shock gas.

4 ATOMIC DATA

The atomic data used for the calculations of the pre-shock gas and hotspot remain the same as in Dodin (2015), except for the electron collisional excitation rates of He_{II} for which more accurate data from Aggarwal et al. (2017) are used.

The following atoms and ions are included in the calculations of the cooling flow: HI-II, HeI-III, CII-VII, NII-VIII, OII-IX, NeII-XI, Mg II-XII, Si II-XIV, S II-XVI, and Fe III-XIX. The atomic data for hydrogen and helium are identical to the data used in the calculation of the hotspot. The remaining atoms and ions are treated in a simplified manner, i.e. the most important low levels are considered explicitly, while the upper levels are combined into superlevels in such a way that the total number of levels for each ion does not exceed 20. Energy levels and radiative atomic data are taken from the NORAD¹ database, compiled by S.N. Nahar, and the TOPbase² (Cunto et al. 1993). About 3000 spectral lines are taken into account in the calculations of the radiative cooling and spectra. Because the photoionization cross-sections include autoionizing resonances, the detailed balance relation gives the total (radiative plus dielectronic) recombination rates for each level. For some ions, the main contribution to the total dielectronic recombination is due to the high lying

¹ http://norad.astronomy.ohio-state.edu

² http://cdsweb.u-strasbg.fr/topbase/topbase.html

levels; however, in the dense plasma of the cooling flow, these levels either do not exist or the recombinations on them are negligible against the high rates of collisional ionization and three-body recombination. Therefore, the total recombination rate to all included levels of an ion must be less than the total recombination rate for the same ion in the interstellar medium.

Collisional excitation and ionization rates are taken from CHIANTI v.7.1 (Dere et al. 1997; Landi et al. 2013) for all available transitions. The rest of the rates are calculated by using approximate formulae from Seaton (1962), Cox (2000), and van Regemorter (1962).

The optimal number of atomic levels for each ion (except ions of hydrogen and helium) is still an open problem. In this regard, we note that significant changes in atomic data used in the calculations of the cooling flow (e.g. different number of atomic levels; all collisional rates are calculated using the approximate formulae or more precise tables) do not lead to noticeable changes in the spectra of the pre-shock gas or the hotspot, while the particular lines in the ionizing spectra can differ by up to a factor of a few. So we suppose that our atomic models are suitable for the calculation of the ionizing radiation, which can be used to model spectra of the pre-shock gas and the hotspot. However, to study the individual spectral lines forming in the cooling flow, separate detailed research of the corresponding atomic models is needed.

5 RESULTS

5.1 Structure and spectrum of the post-shock region

The structure of the cooling flow is calculated for $N_0 = 10^{10} - 10^{14} \text{ cm}^{-3}$, $V_0 = 150 - 500 \text{ km s}^{-1}$, and the solar elemental abundances (Grevesse & Sauval 1998).

The ion fractions in the cooling region for some elements are shown in Fig. 1 for two cases: one where the model (i.e. the temperature, the level populations, the radiation field, etc.) is calculated taking into account departures from the SE, and one where the model is calculated assuming SE. Generally speaking, the differences in the ion fractions reflect not only non-equilibrium effects, but also related changes in the radiation field, which is especially important for the cooled gas, where photoionization by the radiation of overlying layers plays a significant role. However, in practice, this effect turns to be small, because in the hot region, where the ionizing radiation is formed, the departures from SE are small (see Fig. 1). As can be seen from Fig. 1, while the gas cools down, the ion fractions converge to the equilibrium values that allows us to neglect the non-equilibrium effects and consider deeper layers as the hotspot.

Since in this paper we are primarily concerned with helium spectra, we give a more rigorous and quantitative description of the non-equilibrium effects for each level of He II (He I lines are formed mostly in the hotspot). We can simultaneously calculate the non-equilibrium level populations n_i^{neq} and the equilibrium ones n_i^{eq} for a fixed radiation field and other parameters. The ratios $t_i = n_i^{\text{neq}}/n_i^{\text{eq}}$, plotted on Fig. 2, show that the departures from the equilibrium at the lower boundary of the cooling region are less than 10 per cent for all levels.

It is remarkable that there is a smooth transition in the t-factors from the ground state of He II to He III. Only the first excited level is well coupled to the ground state, while the departures from SE of upper levels correspond to the departures of He III due to high rates of collisional ionization and three-body recombination. The most important levels with n=3, 4 show intermediate departures from SE. The non-equilibrium effects are usually considered only

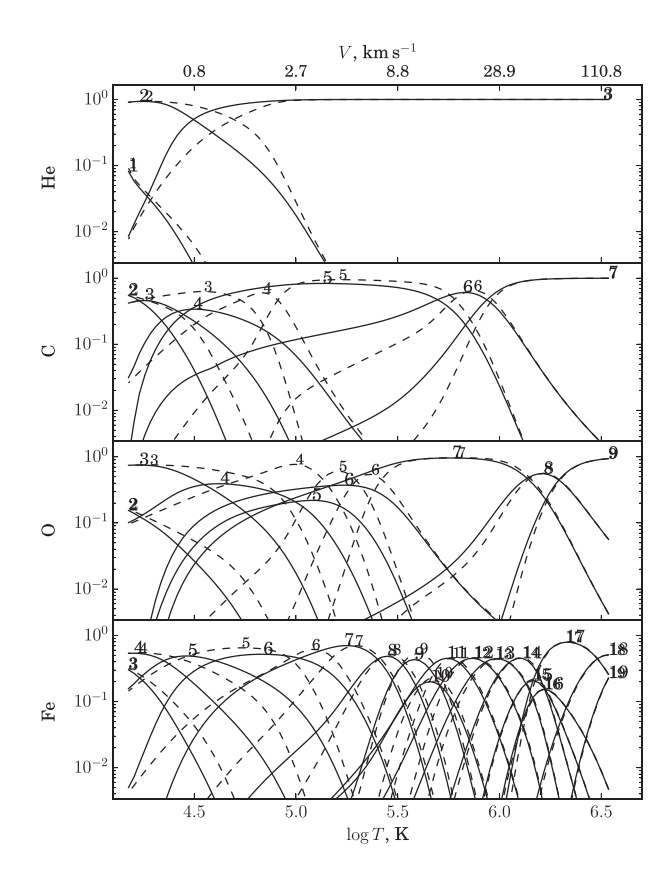


Figure 1. The ion fractions f_i of some elements in the cooling flow for $V_0 = 500 \,\mathrm{km\,s^{-1}}$, $N_0 = 10^{12} \,\mathrm{cm^{-3}}$. The dashed curves and reduced font correspond to the model, calculated assuming SE. The solid lines are for the non-equilibrium level populations. The numbers denote the ionization stages, for example, the number 17 on the lower panel corresponds to the Fe your

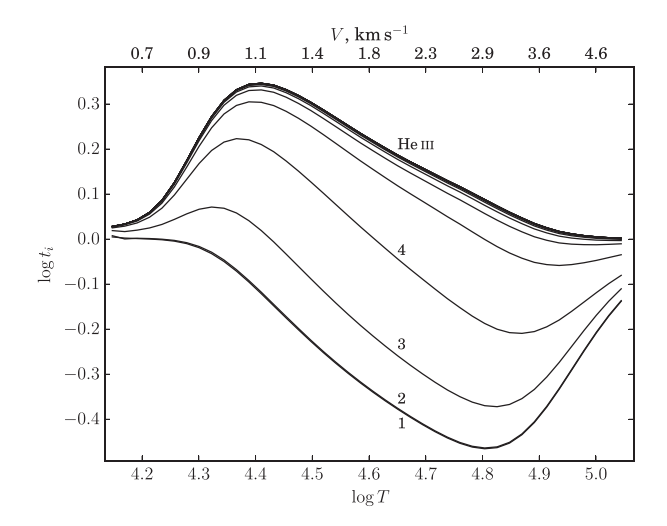


Figure 2. The departures of level populations of He II from the SE $t_i = n_i^{\rm req}/n_i^{\rm eq}$. The structure of the post-shock region is calculated for the non-equilibrium case for $V_0 = 300\,{\rm km\,s^{-1}}$, $N_0 = 10^{12}\,{\rm cm^{-3}}$. The numbers at the curves correspond to the principal quantum number n of the He II levels. The ground state and first excited level have equal departures. The upper line corresponds to the He III ion. The upper axis indicates the gas velocity.

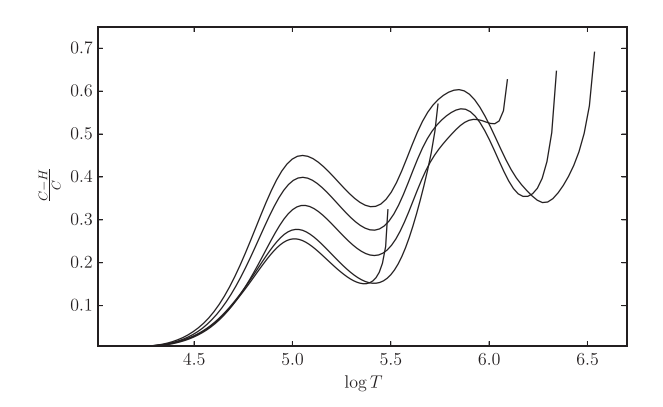


Figure 3. The imbalance between heating H and cooling C of the post-shock gas for the models with $N_0 = 10^{12}$ cm⁻³, $V_0 = 150$, 200, 300, 400, and 500 km s⁻¹.

in calculations of the ion fractions, while the level populations are derived from a balance between collisional excitation from the ground state and radiative decay, i.e. it is assumed that the t-factors of all levels are equal and correspond to the ground state. As can be seen from Fig. 2, in the case of accretion shock this is true only for the first excited level of He $\scriptstyle\rm II$.

The effects of self-irradiation of the cooling flow lead not only to the photoionization of lower layers by upper ones but also to heating. The ratio between the cooling and heating in the cooling flow is shown in Fig. 3.

It can be seen that the balance between the heating and cooling is reached at the lower boundary of the cooling flow, therefore, deeper layers can be considered in the radiative equilibrium, i.e. as the hotspot. The non-monotonicity of the curves is associated with the appearance and disappearance of strong opacity sources. Note that even in the upper layers there is significant heating.

Accounting for the non-equilibrium effects and self-irradiation leads to changes in the cooling curve. We define the net cooling rate as C-H that is the rate of change of total energy E per unit mass due to the radiation (see equations 3–4), while the change of ε is usually included in the cooling rate, therefore, for comparison purposes, we define a quantity

$$\Lambda = \frac{2.11 \times 10^{-24} \,\mathrm{g}}{N_{\mathrm{e}}} \left(C - H + u_0 \frac{\mathrm{d}\varepsilon}{\mathrm{d}m} \right). \tag{9}$$

Note that in the considered problem the contribution of the last term turns out to be small.

The standard cooling curve for a low-density plasma and a few curves for the post-shock region are plotted in Fig. 4. Curve (2) calculated for the equilibrium level populations and without heating (H=0) coincides with the standard one (Curve 1) for $T>10^5$ K. At lower temperatures there are differences, which are caused by the following effects.

We calculate total heating and cooling, which are integrated over all frequencies, including optically thick frequencies, where cooling is well balanced by heating in each grid cell. Therefore, by zeroing the heating, we overestimate the cooling rate that leads to the appearance a hump in Curve (2) at $\log T = 4.5$ in comparison with Curve (1). If these optically thick frequencies are removed from the cooling, then the obtained curve turns out to be similar to the standard one, but the carbon peak at $\log T = 5.0$ is shifted to $\log T = 4.8$, which is caused by photoionization, shifting the ionization equilibrium towards the lower temperatures.

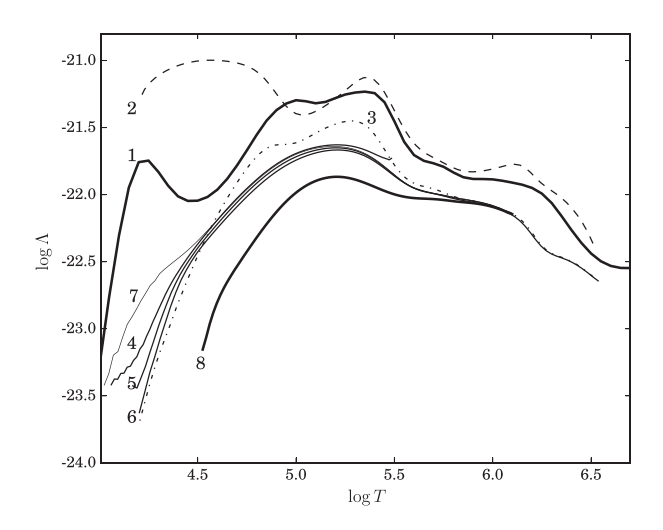


Figure 4. The cooling curves $\Lambda(T)$ (erg s⁻¹ cm³). Curve (1) is the standard cooling curve of astrophysical plasma in the CIE calculated using CHIANTI (the low-density limit, an optically thin gas, no photoionization); (2) is the curve calculated for $V_0 = 500 \, \mathrm{km \, s^{-1}}$, $N_0 = 10^{12} \, \mathrm{cm^{-3}}$ assuming the SE, the heating is ignored H = 0, effects of photoionization and radiative transfer are taken into account; (3) is the same curve, but the heating is included; (4, 5, and 6) are the non-equilibrium curves for $V_0 = 150$, 300, and $500 \, \mathrm{km \, s^{-1}}$, $N_0 = 10^{12} \, \mathrm{cm^{-3}}$; (7 and 8) are the non-equilibrium curves for $V_0 = 300 \, \mathrm{km \, s^{-1}}$, $N_0 = 10^{10}$, $10^{14} \, \mathrm{cm^{-3}}$.

The role of the heating term is illustrated by Curve (3). All the other curves (4–8) correspond to the post-shock region and calculated, accounting for the photoionization, heating, and non-equilibrium effects. The shape of the cooling curve in the non-equilibrium case is generally consistent with the results obtained by Sutherland & Dopita (1993). Increasing the gas density (Curves 7–5–8) increases the heating that reduces the net cooling in the lower layers. Variations of the pre-shock velocity (Curves 4–5–6) practically do not change the cooling curve, which allows the use of the curve calculated for $V_0 = 500 \, \mathrm{km \, s^{-1}}$ as an universal curve instead of the standard one in the time-dependent hydrodynamic modelling of accretion impacts.

The negative slope of the standard cooling curve leads to the shock instability (see Introduction); note in connection with this that at moderate densities, the shape of the cooling curve at $\log T > 5.5$ does not differ significantly from the standard one. Thus, the heating and non-equilibrium effects do not solve the problem of absence of observational evidences of the shock oscillations.

The simple analytical estimate of the vertical scale $L_{\rm post}$ of the post-shock with radiative cooling gives $L_{\rm post} \propto \rho_0^{-1}$ (see e.g. Costa et al. 2017). In principle, an increasing heating with increasing density can distort this relation; however, it turned out that the cooling curve depends on density only at low temperatures $\log T < 5.5$, while the cooling length $L_{\rm post}$ is mostly determined by the high-temperature part of $\Lambda(T)$. This results in the vertical size of the cooling region in our models corresponding to the relation $L_{\rm post} \propto \rho_0^{-1}$ with an accuracy better than 10 per cent.

5.2 Structure and spectrum of the hotspot and the pre-shock gas

In order to calculate the structure and spectrum of the hotspot and the in-falling gas, in addition to the parameters of the shock (N_0, V_0) , the solar elemental abundances), we should define the atmo-

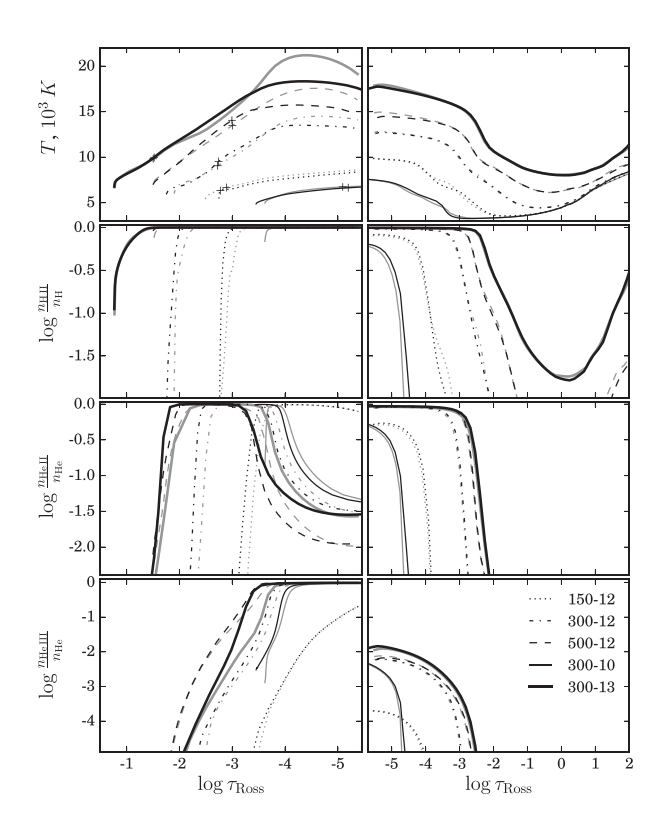


Figure 5. The temperature profiles and ion fractions for hydrogen and helium in the pre-shock region (left-hand panels) and in the hotspot (right-hand panels). The abscissa is the Rosseland-mean optical depth, measured from the shock front for the left-hand panels and the lower boundary of the post-shock region for the right-hand panels. The grey lines are for the HHe model; the black lines are for the HHeCO model. Different line styles are for different accretion parameters, reported in the in the legend by using the notation $V_0 - \log N_0$, where V_0 and N_0 are measured in km s⁻¹ and cm⁻³, respectively. The crosses mark the distance of 10^9 cm from the shock front.

spheric parameters: effective temperature $T_{\rm eff} = 4000 \, \rm K$, surface gravity $\log g = 4.0$, and microturbulence velocity $\xi_t = 2.0 \, \rm km \, s^{-1}$. The post-shock gas radiates equally in both directions except some optically thick lines, for which the flux directed towards the star is smaller than the flux directed towards the in-falling gas. Despite the fact that the densities in the pre-shock gas and hotspot differ by almost three orders of magnitude, the temperatures in both regions turn out to be close.

Fig. 5 shows the temperature profiles and the ion fractions for hydrogen and helium. The typical density profiles for the hotspot can be found in Dodin (2015), and the density in the pre-shock region is constant. The formation region of He I, He II lines for most models is less than 10⁹ cm (except for extreme models of the lowest density $N_0 = 10^{10} \,\mathrm{cm}^{-3}$ and the highest velocity $V_0 = 500 \,\mathrm{km}\,\mathrm{s}^{-1}$), which satisfies our assumptions. As can be seen in Fig. 5, the pre-shock gas is heated up to 10 000-20 000 K, which agrees with earlier calculations (Calvet & Gullbring 1998; Lamzin 1998). The models, shown on the figure by the grey lines, are calculated taking into the account departures from LTE for hydrogen and helium, while the other elements are treated in LTE. We will label this model as HHe. The main non-LTE effect is overionization of ions by the hot radiation from the post-shock, which leads to the appearance of 'hot ions' like He III, which do not correspond to the temperatures, reached in the pre-shock or hotspot. The overionization is reduced

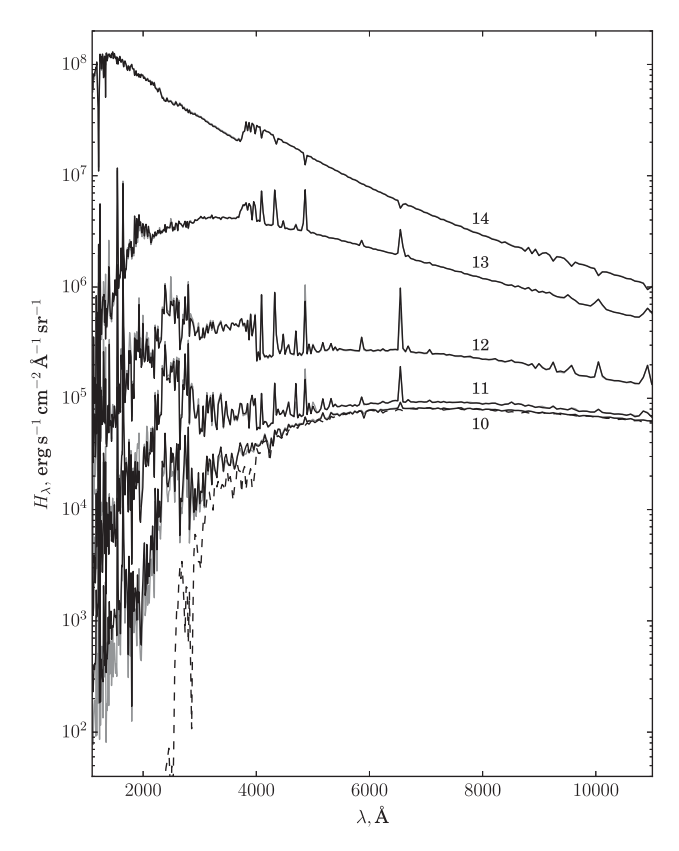


Figure 6. The solid lines are low-resolution ($R \approx 150$) spectra of the accretion region at various $\log N_0$ (indicated by numbers at the corresponding lines) and $V_0 = 300 \, \mathrm{km \, s^{-1}}$. The grey lines are for the HHe model; the black lines are for the HHeCO model. The grey and black lines almost coincide with each other, except for small differences in the UV. The dashed line is for the spectrum of the underlying star with $T_{\rm eff} = 4000 \, \mathrm{K}$ and $\log g = 4.0$.

with increasing density due to three-body recombination putting the populations into LTE. Similar effects must appear not only for H and He, but also for other elements. This can affect the distribution of the physical parameters in the models (T, N_e) , the radiation field J_{ν} , etc.). To estimate changes, induced by non-LTE effects in metals, we include the non-LTE treatment of the ions of C and O, using the compilation of atomic data from Dodin (2015). We will label this model as HHeCO. These models turn out to be cooler by 300–3000 K in the hottest regions near the shock, but slightly hotter (<600 K) in more distant regions. The more important difference is the larger sizes of the hydrogen and helium ionization zones. The comparison of emergent line profiles shows that these changes do not impact the profiles of H I or He I but can enhance the red-shifted component of He II lines (see 5.2.3). A more detailed study of non-LTE effects in metals will be presented in a subsequent work, since in addition to the indirect effect on the He II lines, the metal lines are also of independent interest for the explanation of UV and optical

When the models of the pre-shock region, cooling gas, and hotspot are calculated, they are combined into one and the final outgoing spectrum $I_{\lambda}(\mu)$ is calculated. For presentation purposes, we integrate these intensities to obtain the Eddington fluxes $H_{\lambda} = 0.5 \int_{-1}^{1} I_{\lambda}(\mu) \mu \mathrm{d}\mu$, which are shown in Fig. 6 and for the most important lines, in Fig. 7. Recall that the total flux of a star with the accretion spot can be calculated only when the spot geometry, velocity field, and line of sight are defined. In particular, the shape of the red-shifted component is very sensitive to these parameters.

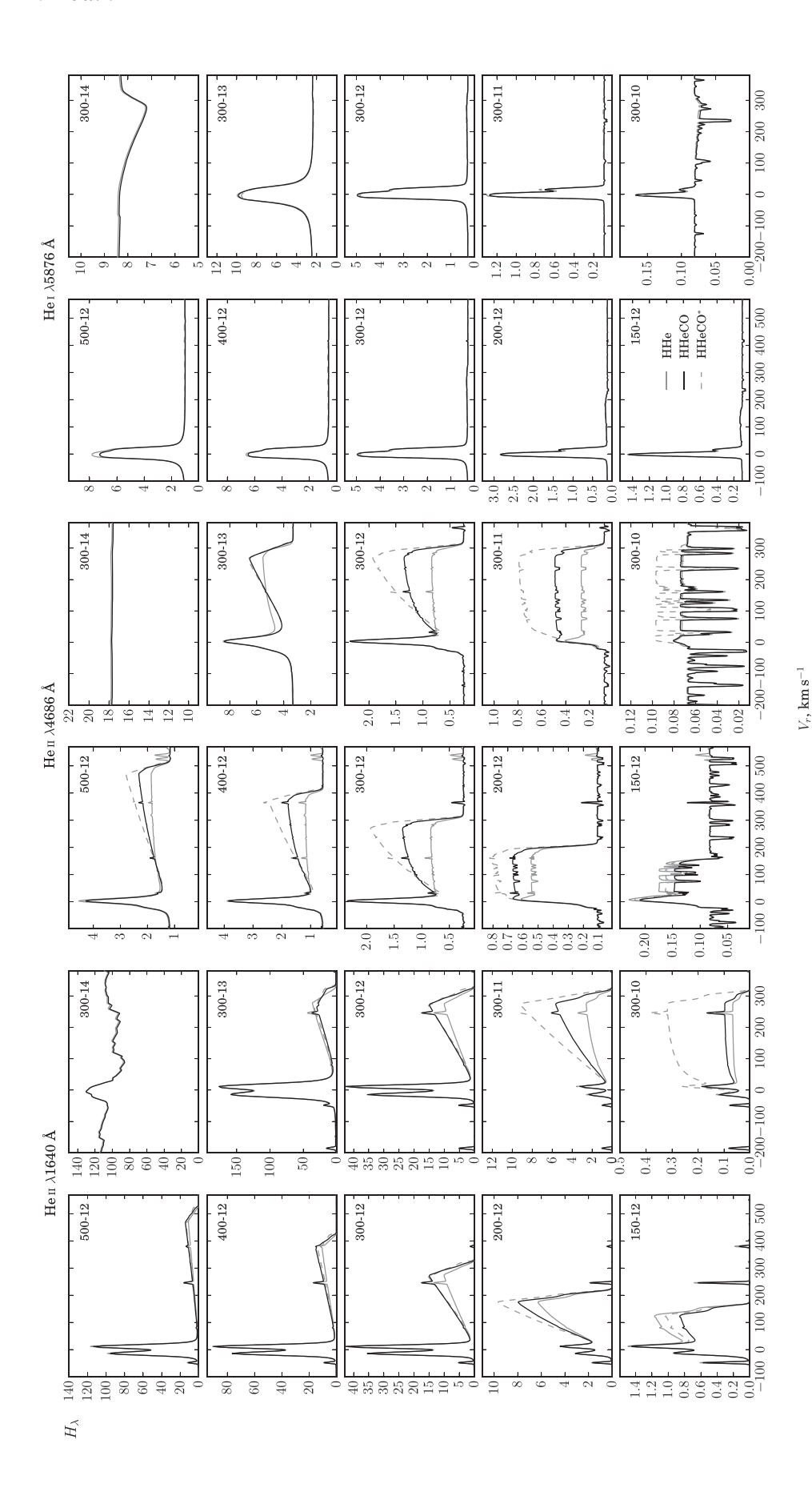


Figure 7. Profiles of some significant lines of He 1 and He 11 for various accretion parameters. The vertical axis is the Eddington flux H_{λ} in 10^6 erg s⁻¹ sm⁻² Å⁻¹ sr⁻¹; the horizontal axis is the radial velocity in km s⁻¹. The left-hand panels are for $N_0 = 10^{12}$ cm⁻³, $V_0 = 150$, 200, 300, 400, and 500 km s⁻¹ (see the $V_0 - \log N_0$ keys in the upper-right-hand corner). The right-hand panels are for $V_0 = 300$ km s⁻¹, $N_0 = 10^{10}$, 10^{11} , 10^{12} , 10^{13} , and 10^{14} cm⁻³. The grey and black solid lines are for HHeCO models, respectively. The dashed lines are for HHeCO* models.

5.2.1 Hydrogen spectrum.

The behaviour of the central component of hydrogen lines coincides with that described in Dodin (2015). In the present work, we take into account the in-falling gas, but in the case of hydrogen lines we do not fully cover the region of their formation, hence the red-shifted component for some models may be underestimated. We will now describe qualitatively the behaviour of the H β line. A weak red-shifted emission is seen at low densities of the infalling gas. Somewhere between the densities N_0 of 10^{12} cm⁻³ and 10¹³ cm⁻³, the emission is replaced by absorption, which is superimposed on the extremely broad central component. At densities $N_0 \sim 10^{14} \, \mathrm{cm}^{-3}$, the central component is completely absorbed in the in-falling gas, in which a deep red-shifted component is formed. Due to the high density, this component is significantly broadened by the Stark effect (FWHM $\approx 600 \, \mathrm{km \, s^{-1}}$). Until now, such broad absorption wings of hydrogen lines have not been observed, which apparently indicates the absence of a very dense gas ($\sim 10^{14} \, \mathrm{cm}^{-3}$) in the accretion columns of CTTS.

The behaviour of the Balmer jump is analogous to the behaviour of hydrogen lines. The emission Balmer jump corresponds to the low-density models, and the absorption Balmer jump is seen at extremely high densities $N_0 \sim 10^{14} \, \mathrm{cm}^{-3}$. The transition from one type to another occurs at $N_0 \sim 10^{13} \, \mathrm{cm}^{-3}$, when the jump does not emerge. This complements results obtained by Calvet and Gullbring (see fig. 3 of Ingleby et al. 2013), where only emission jumps arise.

5.2.2 He I lines.

The results for the narrow component of He I lines are similar to the results of previous work (Dodin 2015). One of the most interesting is that the centre of the He I λ 5876 Å line depends on the accretion parameters. This is due to the fact that the line consists of several fine-structure components, a sequential saturation of which shifts its average position. In Fig. 7, the central wavelength of the lines is taken as the *gf*-weighted average wavelength of all fine-structure components. In addition to this effect, the component can be shifted due to blending with the red-shifted component.

The narrow component of the He I λ 5876 Å line is frequently used to measure the magnetic field in the accretion spots (see for example, Donati et al. 2013; Dodin, Lamzin & Chuntonov 2013). The measured quantity is the longitudinal field weighted with the line intensity. Thus, the angular dependence of the intensity of the He I line is of interest for the interpretation of the obtained results, in particular for (magnetic) Doppler imaging. Our models show that the He I λ 5876 Å line is optically thick, and the intensity $I(\mu)$ in the line centre is almost isotropic.

The He I λ 5876 Å line does not show any significant red-shifted absorption at densities N_0 less than 10^{13} cm⁻³. The absorption appears at higher densities; however, in this case the central component of hydrogen lines reaches a FWHM > 1000 km s⁻¹. The presence of such a broad (but shallow) emission component of hydrogen lines in spectra of CTTS with the red-shifted absorption in lines of He I has not yet been confirmed by observations.

As expected, the in-falling gas turns out to be opaque in the Balmer and Paschen continuum at densities $N_0 \gtrsim 10^{13} \, \mathrm{cm}^{-3}$. The optical thickness of the pre-shock gas in the model with $V_0 = 300 \, \mathrm{km \, s^{-1}}$, $N_0 = 10^{14} \, \mathrm{cm}^{-3}$ is $\tau_{\mathrm{Ross}} > 1$ and strongly depends on the chosen geometrical thickness of the slab. The spectrum of the in-falling gas can be described as a spectrum of a star with an effective temperature $T_{\mathrm{hs}} = (0.5 \rho_0 V_0^3 / \sigma + T_{\mathrm{eff}}^4)^{0.25}$, which is shifted to longer wavelengths.

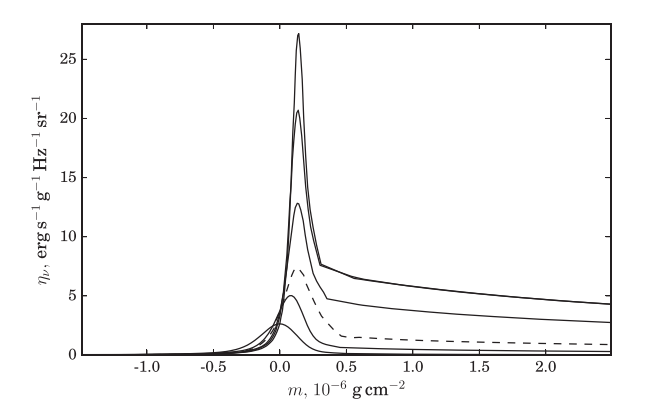


Figure 8. The emission coefficient η_{ν} at the line centre of He II λ 4686 Å. The coordinate origin is located at the point where the settling velocity is equal to $2 \, \mathrm{km \, s^{-1}}$. The shock front is on the left-hand side. The solid lines are for the models with $V_0 = 150$, 200, 300, 400, and $500 \, \mathrm{km \, s^{-1}}$, $N_0 = 10^{12} \, \mathrm{cm^{-3}}$; the dashed line is for the emission coefficient reduced by a factor of 10 for the model with $V_0 = 300 \, \mathrm{km \, s^{-1}}$, $N_0 = 10^{13} \, \mathrm{cm^{-3}}$. For all models, the line is optically thin. It can be seen that the narrow component of the He II λ 4686 Å line is formed at the velocities less than $2 \, \mathrm{km \, s^{-1}}$ (i.e. in the right-hand half of the plot). The distribution of η_{ν} in the case of the He II λ 1640 Å line looks similar.

The He I $\lambda 10830$ Å line shows similar behaviour with the He I $\lambda 5876$ Å line, but the red-shifted component is more pronounced. The red-shifted absorption, a depth of which relative to the continuum is less than 20 per cent, is present at densities $10^{10}-10^{11}$ cm⁻³ and is replaced by a weak emission at densities $10^{12}-10^{13}$ cm⁻³.

5.2.3 He II lines

There is observational evidence that the narrow component of the He II lines is red-shifted by $\sim 10 \,\mathrm{km}\,\mathrm{s}^{-1}$ (see for example, Beristain, Edwards & Kwan 2001; Petrov et al. 2001; Ardila et al. 2013). It is believed that the presence of this shift indicates that the component is formed in the cooling flow. However, our models show that such shifts are impossible in the accepted picture of accretion, because at the settling velocities of $\sim 10 \, \mathrm{km \, s^{-1}}$ the helium is entirely ionized to He III (see Fig. 1). To show where the narrow component is formed in our models, we plot on Fig. 8 the emission coefficient η_{ν} at the line centre of He II λ4686 Å near the conventional boundary between the cooling flow and the hotspot. Note first a smooth transition of η_{ν} between the two regions. The component turns out to be optically thin for all models, therefore the area under the curve is proportional to the flux, and we can conclude that the component is formed at the settling velocities less than $2 \,\mathrm{km}\,\mathrm{s}^{-1}$. If the observed shifts of $\sim 10 \,\mathrm{km}\,\mathrm{s}^{-1}$ are not related to some simple causes, such as blending with other lines or with the red-shifted component, then they may indicate unaccounted effects like the shock instability, two-dimensional effects (Orlando et al. 2010, 2013) or the flow inhomogeneity (Matsakos et al. 2013; Colombo et al. 2016).

He II lines show a significant red-shifted emission. The observed ratios between the red-shifted and central emissions of He II $\lambda 1640\,\mbox{\normalfont\AA}$ line (fig. 17 of Ardila et al. 2013) agree well with our models for a high velocity and moderate density of $\sim\!10^{12}\,\mbox{cm}^{-3}$. Recall that the profiles shown in Fig. 7 correspond to the Eddington flux, in other words, the lines will have such profiles if the whole stellar surface is covered by the accretion spot. The line profiles for different shapes and orientations of the accretion region are different.

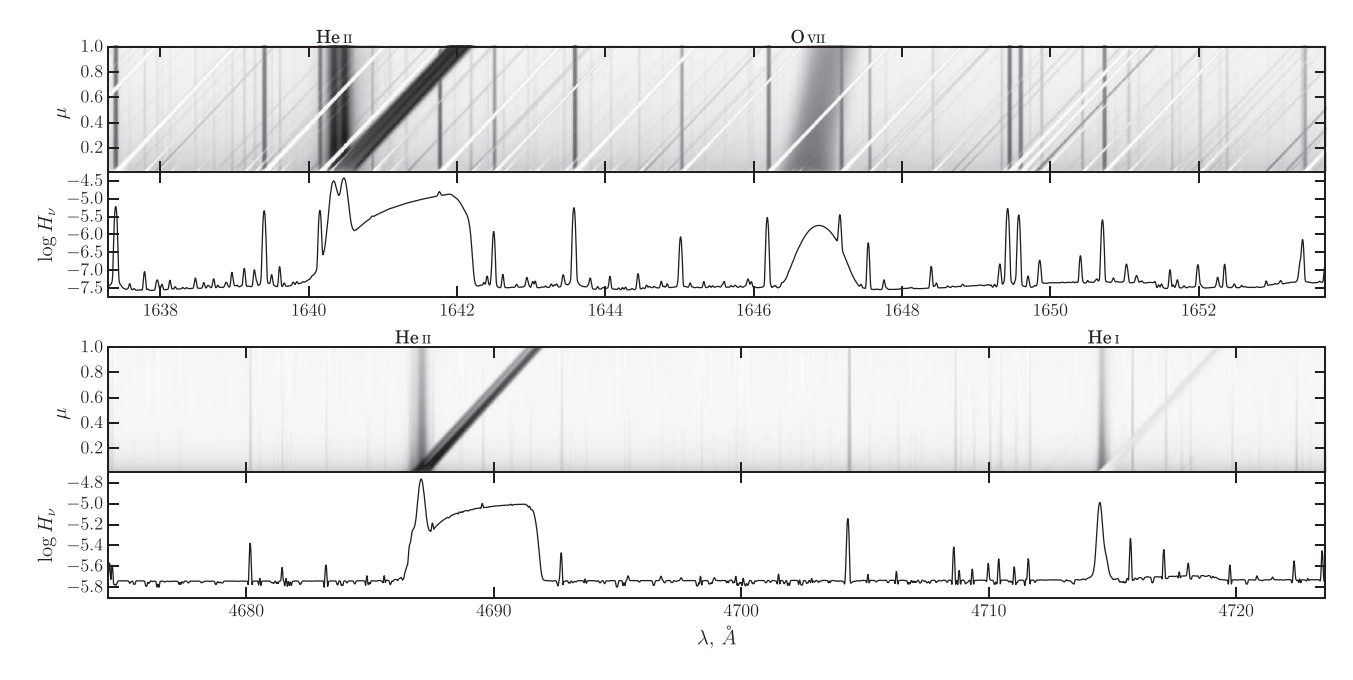


Figure 9. The upper parts of the panels are examples of $I_{\nu}(\mu)$ for the UV and visible spectral ranges for the HHeCO model with $V_0 = 300 \,\mathrm{km \, s^{-1}}$, $N_0 = 10^{12} \,\mathrm{cm^{-3}}$. The inclined strips correspond to the lines that form in the in-falling gas. The flux from the accretion spot is the weighted sum of individual rows, with weights determined by the geometry of the spot. As an example, the Eddington flux (which is proportional to the sum with weights μ) is shown in the bottom parts of the panels. It can be seen that the UV continuum flux is affected by a large number of emission and absorption lines that overlap with each other due to the Doppler effect.

From Fig. 7, we can conclude that if the accretion flow contains only a low-density gas, then the red-shifted component dominates in the profile. It is necessary to note that there is some uncertainty in the intensity of this component due to unaccounted non-LTE effects in metals. The formation region of He II lines depends on how deep the ionizing radiation can penetrate, which depends on the ionization of metals as well as on the ionization of helium itself. The overionization of metals can reduce the opacity for the radiation, which is able to ionize He II that leads to extending the He III zone. Our calculations show that accounting for the non-LTE effects for C and O ions modifies only the red-shifted component of He II lines and only at densities $N_0 \le 10^{12} \, \mathrm{cm}^{-3}$ (see Fig. 7). In order to estimate how the overionization of the other elements can enhance these changes, we calculate the level populations, neglecting in the pre-shock region the opacity due to the elements treated in LTE, which leads to the maximum possible size of the ionization zones of helium ions. The corresponding spectra are shown in Fig. 7 and labelled as HHeCO*.

Let us finally discuss the line-blanketing effect. Significant Doppler shifts related to the in-falling gas lead to strong blending of numerous spectral lines, especially in the UV (see Fig. 9). The blanketing effect grows with increasing density of the in-falling gas and at $N_0 > 10^{13} \, \mathrm{cm}^{-3}$ cannot be ignored even in the visible range.

6 CONCLUSIONS

In this paper, we have adapted the well-developed methods of the theory of stellar atmospheres to model the accretion shock and its surroundings. We have found the following:

(i) The non-equilibrium effects and the self-irradiation modify the shape of the cooling curve only for temperatures $T < 3 \times 10^5$ K. Thus, the unstable part of the cooling curve is not changed. Due

to small non-equilibrium effects at high temperatures, the cooling curve does not depend significantly on the accretion parameters (N_0, V_0) , which allows it to be used in numerical simulations of the instability in the same way as the standard curve.

- (ii) The departures of the populations of excited levels of He $\scriptstyle\rm II$ from the SE for a dense plasma of the cooling flow do not correspond to the departures of the ground state but take intermediate values between the departures of the ground state of He $\scriptstyle\rm II$ and He $\scriptstyle\rm III$.
- (iii) The central as well as the red-shifted component of hydrogen lines is broadened by the Stark effect, which cannot be neglected in gas kinematic studies.
- (iv) The narrow component of the most important helium lines is optically thick, which leads to a shift of the central wavelength of multicomponent lines (e.g. the He $_{\rm I}$ $\lambda 5876$ Å line).
- (v) An unexpected result is the absence of a visible red-shifted absorption in the He I λ 5876 Å line at acceptable accretion parameters, while such an absorption is seen in 4 of 22 CTTS (Beristain et al. 2001). It is probable that this absorption is formed in the accretion column outside the region heated by the shock radiation. However, in this case, we need another ionizing source sufficient for the excitation of helium lines in the accretion column. The probable candidate for the role of the ionizing source may be the coronal X-ray emission (Kurosawa et al. 2011) or the radiation arising at the magnetospheric boundary (Gómez de Castro & von Rekowski 2011).
- (vi) The model of the steady-state accretion shock predicts that the narrow component of He $\scriptstyle\rm II$ line has almost zero radial velocity, while the measurements show a redshift of a few km s⁻¹.Colombo et al. (2016) have suggested a model of fragmented accretion streams and calculated the profiles of C $\scriptstyle\rm IV$, which show significant Doppler shifts. It is possible that a similar mechanism is responsible for the observed shifts of the narrow component of He $\scriptstyle\rm II$. However, it is necessary to note that Colombo et al. (2016) have used the approximation of the collisional ionization equilibrium (CIE), while

we have seen that the non-equilibrium effects and photoionization shift the formation region of the C IV lines towards the lower temperatures. Namely the peak ion fraction of C IV in the CIE case is achieved at 10^5 K (the CHIANTI calculations), while accounting for the above-mentioned effects shifts it to 3×10^4 K (see Fig. 1).

(vii) The observed two-component profiles of He II $\lambda 1640 \text{ Å}$ line agree well with the modelled ones calculated for a high velocity $V_0 = 400$ – $500 \, \mathrm{km \, s^{-1}}$ and moderate density of $N_0 \sim 10^{12} \, \mathrm{cm^{-3}}$. It motivates performing similar calculations for other elements (primarily C, N, O), lines of which show red-shifted features, because the strong dependence of the shape of such profiles on the flow geometry opens new possibilities for the diagnostics of the accretion zone.

The cooling curves and intensities $I_{\nu}(\mu)$ for hydrogen and helium lines are publicly available via the project website http://lnfm1.sai.msu.ru/~davnv/hotspot.

ACKNOWLEDGEMENTS

The author thanks an anonymous referee for valuable comments and suggestions, which have improved this manuscript. The reported study was funded by Russian Foundation for Basic Research according to the research project 16-32-00794 mol_a.

REFERENCES

Aggarwal K., Igarashi A., Keenan F., Nakazaki S., 2017, Atoms, 5, 19

Alencar S. H. P. et al., 2012, A&A, 541, A116

Ardila D. R. et al., 2013, ApJS, 207, 1

Beristain G., Edwards S., Kwan J., 2001, ApJ, 551, 1037

Blinova A. A., Romanova M. M., Lovelace R. V. E., 2016, MNRAS, 459, 2354

Brown P. N., Byrne G. D., Hindmarsh A. C., 1989, SIAM J. Sci. Stat. Comput., 10, 1038

Calvet N., Gullbring E., 1998, ApJ, 509, 802

Colombo S., Orlando S., Peres G., Argiroffi C., Reale F., 2016, A&A, 594, A93

Costa G., Orlando S., Peres G., Argiroffi C., Bonito R., 2017, A&A, 597, A1

Cox A. N., 2000, Allen's Astrophysical Quantities, 4th edn. Springer-Verlag,

Cunto W., Mendoza C., Ochsenbein F., Zeippen C. J., 1993, A&A, 275, L5Dere K. P., Landi E., Mason H. E., Monsignori Fossi B. C., Young P. R.,1997, A&AS, 125

Dodin A. V., 2015, Astron. Lett., 41, 196

Dodin A., 2017, in Balega Y. Y., Kudryavtsev D. O., Romanyuk I. I., Yakunin I. A., eds, ASP Conf. Ser. Vol. 510, Stars: From Collapse to Collapse. Astron. Soc. Pac., San Francisco, p. 110

Dodin A. V., Lamzin S. A., 2012, Astron. Lett., 38, 649

Dodin A. V., Lamzin S. A., Chuntonov G. A., 2013, Astrophys. Bull., 68, 177

Donati J.-F. et al., 2007, MNRAS, 380, 1297

Donati J.-F. et al., 2008, MNRAS, 386, 1234

Donati J.-F. et al., 2011, MNRAS, 412, 2454

Donati J.-F. et al., 2013, MNRAS, 436, 881

Drake J. J., Ratzlaff P. W., Laming J. M., Raymond J., 2009, ApJ, 703, 1224 Gómez de Castro A. I., von Rekowski B., 2011, MNRAS, 411, 849

Grevesse N., Sauval A. J., 1998, Space Sci. Rev., 85, 161

Günther H. M. et al., 2010, A&A, 518, A54

Hartmann L., Herczeg G., Calvet N., 2016, ARA&A, 54, 135

Ingleby L. et al., 2013, ApJ, 767, 112

Koenigl A., 1991, ApJ, 370, L39

Koldoba A. V., Ustyugova G. V., Romanova M. M., Lovelace R. V. E., 2008, MNRAS, 388, 357

Kurosawa R., Romanova M. M., 2013, MNRAS, 431, 2673

Kurosawa R., Romanova M. M., Harries T. J., 2011, MNRAS, 416, 2623

Lamzin S. A., 1995, A&A, 295, L20

Lamzin S. A., 1998, Astron. Rep., 42, 322

Lamzin S. A., 2003, Astron. Rep., 47, 498

Landi E., Young P. R., Dere K. P., Del Zanna G., Mason H. E., 2013, ApJ, 763, 86

Matsakos T. et al., 2013, A&A, 557, A69

Muzerolle J., Calvet N., Hartmann L., 2001, ApJ, 550, 944

Olson G. L., Kunasz P. B., 1987, J. Quant. Spec. Radiat. Transf., 38, 325

Orlando S., Sacco G. G., Argiroffi C., Reale F., Peres G., Maggio A., 2010, A&A, 510, A71

Orlando S. et al., 2013, A&A, 559, A127

Petrov P. P., Gahm G. F., Gameiro J. F., Duemmler R., Ilyin I. V., Laakkonen T., Lago M. T. V. T., Tuominen I., 2001, A&A, 369, 993

Piskunov N. E., Tuominen I., Vilhu O., 1990, A&A, 230, 363

Romanova M. M., Ustyugova G. V., Koldoba A. V., Wick J. V., Lovelace R. V. E., 2003, ApJ, 595, 1009

Sacco G. G., Argiroffi C., Orlando S., Maggio A., Peres G., Reale F., 2008, A&A, 491, L17

Seaton M., 1962, Atomic and Molecular Processes. Academic Press, New York

Sutherland R. S., Dopita M. A., 1993, ApJS, 88, 253 van Regemorter H., 1962, ApJ, 136, 906

APPENDIX A: THE JUMP CONDITIONS

To obtain the gas parameters in the first point behind the shock front, we rewrite the conservation equations (1)–(4) as

$$\rho_{\rm in}V_{\rm in} = \rho_0 V_0,\tag{A1}$$

$$P_{\rm in} + \rho_{\rm in} V_{\rm in}^2 = \rho_0 V_0^2 + P_0, \tag{A2}$$

$$\frac{V_{\text{in}}^2}{2} + \frac{5}{2} \frac{P_{\text{in}}}{\rho_{\text{in}}} + \varepsilon_{\text{in}} = \frac{V_0^2}{2} + \frac{5}{2} \frac{P_0}{\rho_0} + \varepsilon_0. \tag{A3}$$

The indices '0' and 'in' denote the last point of the pre-shock and the first point of the hotspot. We assume that between these states the gas does not lose energy via the radiation, but becomes ionized, i.e. the part of its thermal energy converted to ε . Expressing $\rho_{\rm in}$ from equation (A1), $P_{\rm in}$ from equation (A2) and substituting them in equation (A3), we obtain

$$\frac{V_{\rm in}^2}{2} + \frac{5}{2}(V_0 - V_{\rm in})V_{\rm in} + \frac{5}{2}\frac{P_0}{\rho_0}\frac{V_{\rm in}}{V_0} + \varepsilon_{\rm in} = \frac{V_0^2}{2} + \frac{5}{2}\frac{P_0}{\rho_0} + \varepsilon_0.$$
 (A4)

If we introduce the variables

$$x = \frac{V_{\text{in}}}{V_0}, \qquad A = \frac{P_0}{\rho_0 V_0^2}, \qquad B = \frac{\varepsilon_{\text{in}} - \varepsilon_0}{V_0^2},$$
 (A5)

then equation (A4) is transformed to the form

$$x^{2} - \frac{5}{4}(1+A)x + \frac{1}{4} + \frac{5}{4}A - \frac{1}{2}B = 0.$$
 (A6)

Note that in our case $A, B \ll 1$, then, solving the quadratic equation and retaining only first order terms, we obtain

$$x_1 \approx 1 + \frac{2}{3}B, \qquad x_2 \approx \frac{1}{4}\left(1 + 5A - \frac{8}{3}B\right).$$
 (A7)

The shock wave corresponds to the second root. The parameters ρ_{in} and P_{in} can be obtained by substituting the initial velocity $V_{\text{in}} = x_2 V_0$ in equations (A1) and (A2).

This paper has been typeset from a TEX/IATEX file prepared by the author.